Soft Matter

Poroviscoelasto-plasticity of agarose-based hydrogels

Journal:	*Soft Matter*
Manuscript ID	SM-ART-10-2022-001356.R1
Article Type:	Paper
Date Submitted by the Author:	02-Dec-2022
Complete List of Authors:	Crespo-Cuevas, Victor; University of Colorado Boulder College of Engineering and Applied Science, Mechanical Engineering Ferguson, Virginia; University of Colorado Boulder, Mechanical Engineering Vernerey, Franck; University of Coloroad at Boulder, Mechanical Engineering

Poroviscoelasto-plasticity of agarose-based hydrogels

Victor Crespo-Cuevas, Virginia L. Ferguson, Franck Vernerey

Department of Mechanical Engineering, University of Colorado Boulder, Boulder, CO, 80309 USA
victor.crespo@colorado.edu, virginia.ferguson@colorado.edu, franck.vernerey@colorado.edu

Keywords: Agarose gels, Multi-step stress relaxation, Creep, Poroviscoelasto-plasticity, Abaqus, Transient Network Theory

ABSTRACT

Agarose gels are excellent candidates for tissue engineering as they are tunable, viscoelastic, and show a pronounced strain-stiffening response. These characteristics make them ideal to create *in vitro* environments to grow cells and develop tissues. As many other biopolymers, viscoelasticity and poroelasticity coexist as time-dependent behaviors in agarose gels. While the viscoelastic behavior of these hydrogels has been considered using both phenomenological and continuum models, there remains a lack of connection between the underlying physics and the macroscopic material response. Through a finite element analysis and complimentary experiments, we evaluated the complex time-dependent mechanical response of agarose gels in various conditions. We then conceptualized these gels as a dynamic network where the global dissociation/association rate of intermolecular bonds is described as a combination of a fast rate native to double helices forming between aligned agarose molecules and a slow rate of the agarose molecules present in the clusters. Using the foundation of the transient network theory, we developed a physics-based constitutive model that accurately describes agarose behavior. Integrating experimental results and model prediction, we demonstrated that the fast dissociation/association rate follows a nonlinear force-dependent response, whose exponential evolution agrees with Eyring's model based on the transition state theory. Overall, our results establish a more accurate understanding of the time-dependent mechanics of agarose gels and provide a model that can inform design of a variety of biopolymers with a similar network topology.

1. INTRODUCTION

Biopolymers are used extensively as both commodity materials and for specialized applications[1–3]. For example, chitin is important for medical devices and wound-healing dressings[4], carrageenan films play an important role in extending the shelf life of foods[5], alginate is used to prevent dehydration of meats[6], and agar is common for culturing cells[7–9]. Biopolymers are selected for their ease of manufacture from natural precursor materials as well as for their ability to bear loads over long time scales. However, biopolymers also exhibit complex behaviors that may influence their durability and function. An accurate characterization of these materials is thus critical to guide material selection and design, yet many aspects of how biopolymers respond to loads applied over time remain poorly understood. Their physical behaviors are complex and vary across multiple length scales[10], where many behave as semiflexible networks. Typically, these polymeric systems have supramolecular assemblies which can vary between about one nanometer and tens of nanometers. Of particular interest are agarose-based hydrogels, which are commonly used as scaffolds in tissue engineering due to their low cost, biodegradability, and highly controllable elastic properties[11]. Agarose gels are viscoelastic semiflexible biopolymer hydrogels whose mechanical response depends on the polymer concentration[12] and has been demonstrated to exhibit a strain stiffening response that is likely to influence cellular responses[13,14]. While bulk properties are important to bear loads, cells respond directly to the small-length scale properties and behavior of their host scaffolds. Modulus, viscoelasticity, plasticity, and nonlinear elasticity of substrates and scaffolds influence cells and alter the fundamental processes of growth, proliferation, migration, and differentiation[15,16].

To better understand the characteristic mechanics and time-dependent response of agarose gels, let us first describe its network features. Below the gelation point, double helices are formed through the conglomeration of agarose molecules.

Each agarose molecule participates in more than one double helix. Supramolecular fibers form from the aggregation of double helices through hydrogen bonding. These bonds govern the self-gelation of agarose gels (Figure 1.A) and enable the network to be dynamic through bond formation and dissociation which dissipates elastic stored energy when exposed to mechanical stimuli. The agarose molecules within the supramolecular fibers of the network structure thus possess a solid-like behavior that has been proposed to be capable of fast energy dissipation. In contrast, agarose molecules present in the clusters or junctions and that are not aligned can dissipate energy much more easily as they slide over adjacent molecules thus generating a fluid-like behavior[17]. Hence, it has been proposed that bond exchange processes taking place in the junctions will correspond to longer relaxation times or slower dissipation of the stored elastic energy. Clusters formed by several suprafibers within agarose networks increase the number of connected bonds under deformation. The adjacent agarose molecules that are not part of the cluster in a stress-free configuration are then able to form new crosslinks which increases the size of the cluster and strengthens the network. This process enables agarose to dissipate stress when loaded over long time periods. Elucidating the complex behavior of agarose gels is crucial to design more controllable materials, but also to elucidate the factors leading to cell responses when subjected to externally applied loads. In addition, a deeper understanding of agarose behavior will provide novel insight into many biological materials which present similar network topology (i.e., actin filaments and collagen gels) (Figure 1.B).

The behavior of agarose gels, and many other biopolymers, is considered to be poroviscoelastic because of their high-water content[18–20]. Fluid movement and mass transport through the solid network influence behavior. However, existing poroviscoelastic models fail to connect the network topology with the mechanical response of the solid phase within hydrogels. Such models lack accuracy as they do not account for the movement and rearrangement of molecules within the polymer network. Generally, existing mathematical models used to characterize the macroscopic mechanical response of agarose are empirical. Most either describe the mechanical response by approximating its structure as a combination of simple linear elements (i.e., Maxwell or Kelvin-Voigt model) or describe the stress-strain relations from the stored elastic energy expressions (i.e., Neo-Hookean or Holzapfel model). Studies using a linear combination of phenomenological models, such as Prony series viscoelastic model[21], can broadly be found in literature to describe the time-dependent response of agarose-based hydrogels. For example, Chen *et al.* (2011)[22] used this approach to study the deformation of chondrocytes seeded in agarose gels while Pauly *et al*. (2017)[23] investigated the effects of additives on the mechanical properties of agarose hydrogels. On the other hand, Caccavo and Lamberti (2017)[24] used fundamental balance laws to describe the poroviscoelastic behavior of hydrogels under large deformation, and applied it to agarose-based hydrogels[25]. This latter model provided an important step towards the development of refined models for biopolymers; however, this modeling approach is empirical which limits its use for design purposes. High-precision atomistic simulations, such as molecular dynamics, have been the subject of an increasing developments in the last two decades. The molecular modeling of hydrogels incorporates into a model every single element that is part of the system (i.e., atomic positions, velocities, and forces). In this context, Casalini (2013)[26] developed a molecular model of an agarose-carbomer hydrogel to explore the effect of mesh size on solvent diffusion at low solute concentration. Although atomistic models remove all the assumptions that limit the application of a specific model, they are still computationally expensive and difficult to apply to polymeric networks models at large time scales. Thus, while viscoelasticity in agarose networks have been studied extensively, no studies to date evaluate if the time-dependent response of hydrogels can be accurately described by dynamic bond evolution.

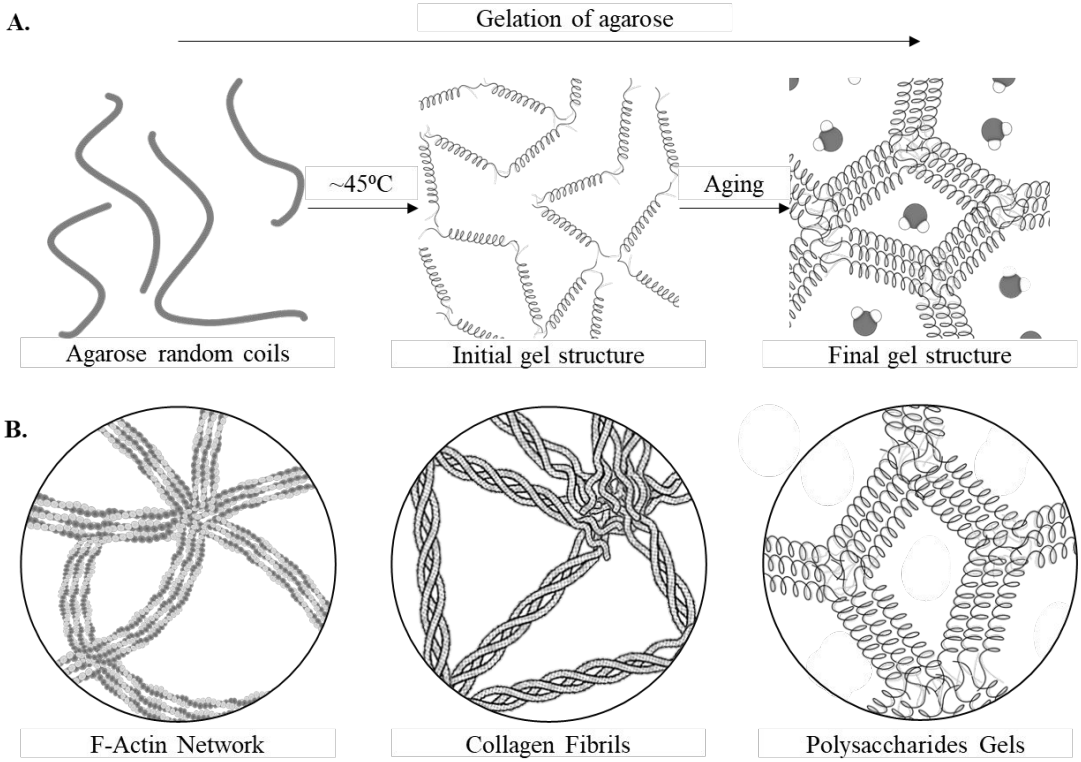

Figure 1. A. Gelation mechanism of agarose, from left to right: When water is added to agarose and it is heated up, agarose untangle and forms random coils. As the agarose cools (~45ºC), coils pair to form helices. As the temperature continues to drop, the helices bundle and form higher-order assemblies (suprafibers) that are coincident with water inside the gel. **B**. Schematic representation of different biopolymer network showing cluster and thick fibers structure.

In this study, we connect the viscoelastic macroscopic response with the chain-level physics of agarose-based hydrogels. This work seeks to establish a fundamental understanding of mechanisms responsible for nonlinear viscoelasticity of agarose hydrogels by adapting the Transient Network Theory (TNT)[27] to the case of agarose networks. More specifically, the TNT is modified to capture the force-dependent response of the fast bond dynamics observed during creep and to capture the nonlinear plastic flow-like behavior observed during the multi-step stress-relaxation experiment. We propose bond dynamics as a novel mechanism for describing strain-stiffening and force-dependent viscoelastic material behavior of agarose. With new data we sought to better understand the time-dependent mechanics of agarose gels to inform their design and to provide a model that may be extended to a range of biopolymers which share similar network topology. The manuscript is organized as follows. In Section 2, we present and analyze experimental results on the behavior of agarose subjected to unconfined compression and study the poroelastic contribution on the overall time-dependent response. In Section 3 we review the main elements of the TNT to model the response of dynamic polymer networks and introduce the nonlinear bond dynamics of agarose-based gels based on network topology. We then modify the TNT to capture the experimental observations reported in Section 2. Finally, in Section 4, we provide a comprehensive overview of the model.

2. CHARACTERIZATION OF THE TIME-DEPENDENT RESPONSE OF AGAROSE UNDER UNCONFINED COMPRESSION

In this section, we present and analyze experimental results on the behavior of agarose subjected to unconfined compression. We described the time-dependent mechanical response of agarose gels for multi-step stress-relaxation and steady creep conditions with the objective of establishing a connection with chain-level physics. Because agarose is a biphasic material comprised of a solvent-filled biopolymer network, we first aimed to characterize the role of poroelastic effects, i.e., the time dependence of the response related to solvent transport, on the gel's overall response. Thus, finite element analysis (FEA) was used to model and reproduce fluid transport in experimental specimens during loading over time.

2.1 Experimental methodology

Agarose Gel Fabrication. Hydrogels were prepared by dissolving 5%, 7.5% and 10%, (w/w) agarose (Sigma A9539) into phosphate buffered saline (PBS, pH 7.4, Invitrogen), and while stirring the agarose powder was slowly added to prevent clumping. The solution was weighed, covered with aluminum foil to reduce evaporation, and boiled (~95^{o}C) and magnetically stirred to maintain homogeneity for 5-10 minutes until agarose was dissolved. Agarose solutions were drawn into 3-, 5-, and 10-ml syringes cooled at room temperature. The hydrogels were removed from the syringes and cut into 8.66 mm, 12 mm and 16 mm lengths, respectively, to create 1:1 cylinders (height:diameter ratio).

Unconfined Compressive Multi-step Stress-Relaxation Test. A total of 15 samples were swelled to equilibrium in PBS for 48 h. Unconfined Compressive stress-relaxation testing (n = 3 samples/composition/dimension) was conducted on a Mechanical Testing System (MTS Insight II; Eden Prairie, MN; 250 N load cell; data recorded at 1 Hz) at room temperature; testing was performed with samples immersed in PBS. Aluminum compression platens were rigid, impermeable, and smooth. A minimum contact force of 30 mN ensured full contact between platen and sample (Figure 2.A). A USB-camera (Dino-Lite 1.3MP EdgePLUS AM4117MZT) was used to assess for full contact prior to testing as well as to evaluate uncompressed, fully compressed, and recovered (48 hours of swelling after testing) dimensions to calculate lateral expansion. The test profile included four incremental steps in strain ϵ = {5%, 10%, 15%, 20%}. Each of these stages was divided into a compression phase and a relaxation phase. Samples were deformed at a strain rate of $\dot{\epsilon}$ = 0.05/s over 1 s, and then each strain was held for 5 h to reach an equilibrium stress state (Figure 2.B).

Water absorption/release quantification. After swelling in PBS for 48 hours, 5% w/w samples (n = 3) were weighed for initial mass m_0 (before mechanical testing and final mass m_f (after stress-relaxation experiments). Samples were weighed quickly to avoid water reabsorption and minimize evaporation, and the amount Δm of solvent exchanged with the media Δm was calculated. This procedure was used for the lower agarose concentration gels since their higher porosity (Table 1) made them best candidates to have larger values for Δm. Samples were next re-submerged in PBS and weighed after 48 hours to assess for mass of fluid reabsorbed.

Unconfined Compressive Creep Test. Unconfined compressive creep tests were also conducted to evaluate short-term time-dependent responses. Creep testing was performed in PBS at room temperature on an MTS with closed-loop load control. A total of 9, cylindrical, 12x12 mm samples (n = 3/group) were subjected to constant compressive stress based on the overall strains achieved after a fast-loading stage ($\dot{\epsilon}_l$ = 0.05/s.). The overall strains achieved during the loading stage were ϵ_l = {1%, 2.5%, 5%, 7.5%, 10%, 15%}. The loading stage was followed by a 120 s creep hold at ϵ_l.

2.2 Experimental approach: multi-step stress-relaxation

The multi-step stress relaxation depicted in Figure 2. C-E shows the mean stress versus time response of the three different sample sizes for each of the three agarose gels compositions. At each level of applied strain, the stress increased immediately after the step-strain application, followed by a relaxation stage that reaches a quasi-steady value, referred to as the plateau stress σ_p in the remainder of the manuscript. We observed that this value increases with the applied strain while being independent of specimen size. Equilibrium values for the stress at the end of the stress-relaxation testing were determined

to be 0.028 ± 0.00082 MPa, 0.055 ± 0.0011 MPa and 0.083 ± 0.0005 MPa for 5% w/w, 7.5% w/w and 10% w/w respectively. The stress relaxation data were consistent between different samples showing a small variability.

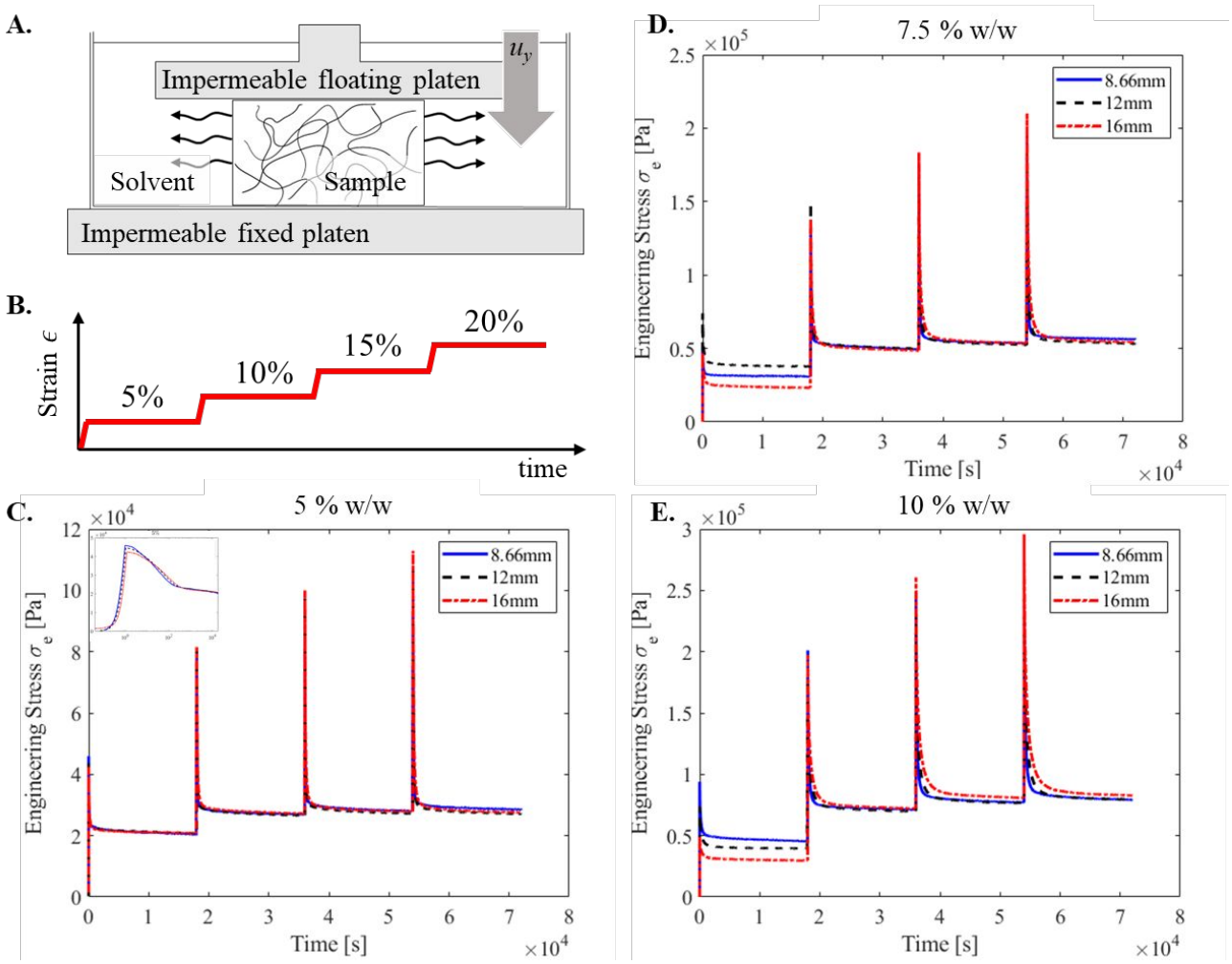

Figure 2. **A**. Schematic of the unconfined compression test of a cylindrical disk of hydrated hydrogel. **B**. Strain vs. time function features multiple steps with holding times to observe relaxation. **C**, **D,** and **E.** Experimental results obtained from multi-step stress-relaxation (8.66 mm, 12 mm, and 16 mm) for 5%, 7.5%, and 10% w/w agarose compositions, respectively. For each dimension, the averaged data is represented. For each composition, agarose gels showed the same long-term stress-relaxation response independent of the sample size. The inset in **C**. shows the stress evolution for the first loading and relaxation step in a semilogarithmic scale along the x-axis.

A similar "stress-plateau effect" behavior was observed in multi-step stress relaxation testing (with a 30 minute relaxation period) on the data reported by Roberts *et al.* (2011)[12] in their comparative study of the viscoelastic mechanical behavior of agarose and poly(ethylene glycol) hydrogels. Because of the relatively short time used between step strains in this previous study, the stress does not plateau as clearly as reported here although general trends are constant between the two studies.

2.3. Experimental approach: steady-state creep.

When subjected to a constant compressive load, the agarose sample displayed a combination of elastic deformation and creep as described below and as shown in Fig. 3.A. First, following a period of fast elastic deformation, the specimen displayed a transitory regime where creep rate first substantially decreased with respect the loading rate $\dot{\epsilon} = 0.05/s$ and then later increased before reaching a steady-state creep (Figure 3.C). We also observed a convergence of the strain rate to a constant over time, which indicated steady-state creep and not consolidation effects from fluid transport out of the gel. We further noted that the average creep rate increased with applied stress (Figure 3.B), suggesting that the creep response of

agarose is force dependent. At higher loads, however, creep could only be sustained for a while before the specimen ruptures. We finally did not notice major differences between the creep response of agarose with different compositions.

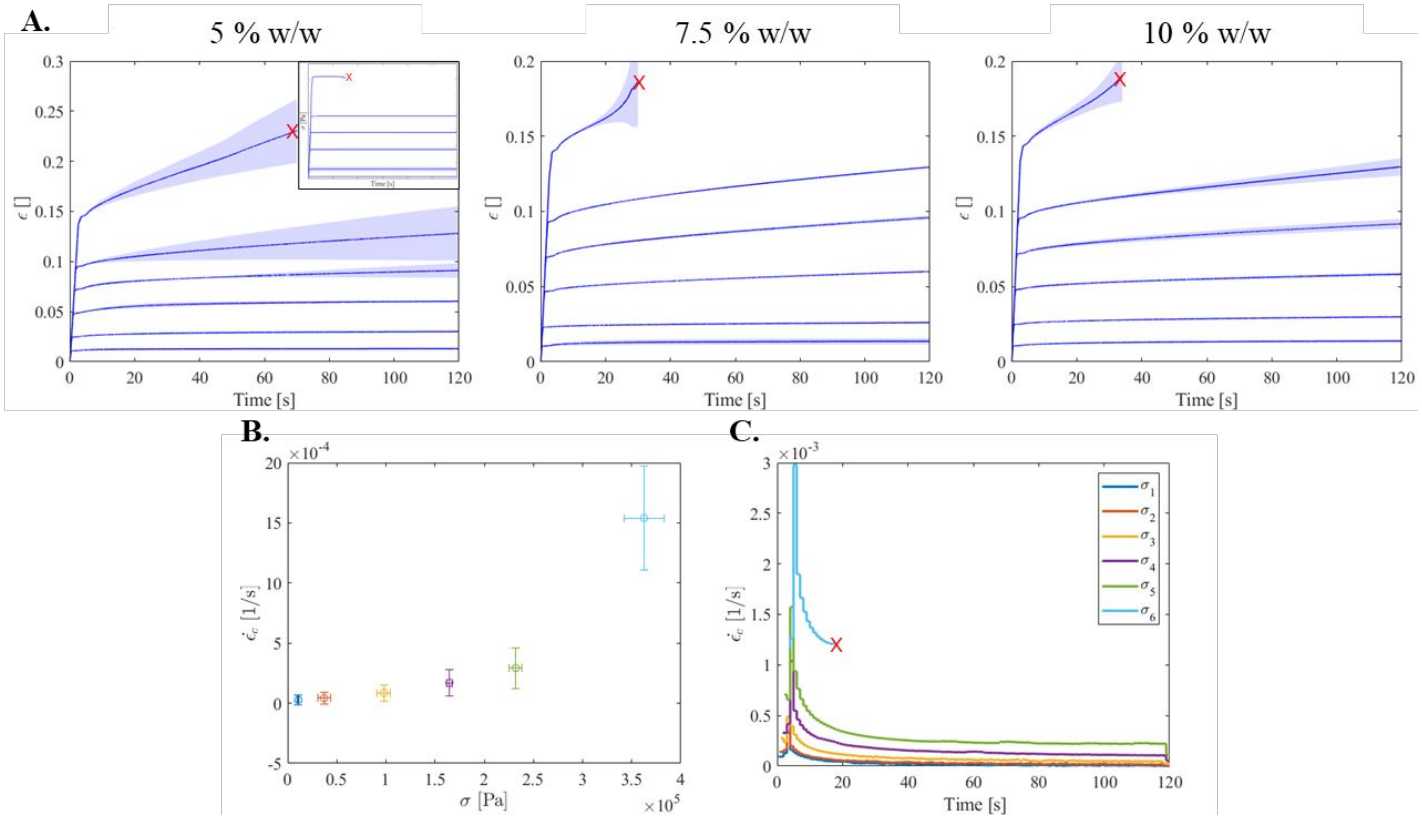

Figure 3. A. Experimental results obtained from creep tests of 12 mm height (and diameter) samples for each of the agarose compositions (n = 3/composition). Data is reported using a solid blue line (average values from samples tested), and a blue region (± standard deviation). The red-cross indicates mechanical failure. Agarose gels showed same creep response independent of agarose composition. **B.** Evolution of the average data for the creep strain rate $\dot{\epsilon}_c$ respect the average data of the constant stress applied σ_i ($\sigma_1 < ... < \sigma_6$) during the creep test. **C.** Evolution of the average data for the creep strain rate $\dot{\epsilon}_c$ over time for the different constant stresses applied σ_i. Red-cross indicates the mechanical failure.

2.4. Poromechanical effects

As most biopolymers, agarose can be considered as a biphasic mixture consisting of two constituents: a solid skeleton phase that is intermixed with a fluid phase. In the following, we therefore use superscripts s and f to denote the solid and fluid phases, respectively[18,28,29]. For simplicity, the solid matrix is assumed to have an isotropic and uniform pore distribution on the whole domain while the mixture is assumed to have reached its equilibrium swollen state so it can be considered fully saturated. During deformation, however, the fluid can move relative to the solid skeleton, producing an effective time-dependence of the mixture, independently of the material response of the polymer matrix. This poroelastic effect brings a challenge to data interpretation as it is difficult to decouple the viscoelastic and poroelastic origins of the material's time behavior[30–33]. The volume fraction $n^\alpha(\boldsymbol{X},t)$ of phase α ($\alpha = s$ or f) is defined as $n^\alpha(\boldsymbol{X},t) = \frac{dv_\alpha}{dv}$, where $\boldsymbol{X}$ is the material coordinate, t is the time, and dv_α is the differential volume fraction of constituent α. The saturation condition implies that $n^s + n^f = 1$ and the total Cauchy stress can be decomposed into a solid and fluid component as[34]:

$$\boldsymbol{\sigma} = \boldsymbol{\sigma^s} + \boldsymbol{\sigma^f} = \boldsymbol{\sigma^s} - p^f \boldsymbol{I} \quad (1)$$

Here, p^f stands for the fluid pressure, $\boldsymbol{\sigma^s}$ is partial stress of solid skeleton[35] and $\boldsymbol{I}$ is the identity tensor. Interstitial fluid flow is modeled based on isotropic Darcy's law as $\nabla p^f = -\frac{1}{K}\frac{e}{1+e}(v^f - v^s)$[36] where e is the void ratio, K is the hydraulic conductance, v^s is the velocity of the solid phase and v^f is the velocity of the fluid phase, as before.

To explore the extent of these effects on material response, we implemented the above linear poromechanics model into a general-purpose FEA software Abaqus 2019 (Dassault Systèmes Simulia Corp., USA). The specimen was modeled as an axisymmetric cylinder around its axis of revolution (r = 0) (Figure 5.B). Solvent transport was assumed isotropic and modeled by defining the hydraulic conductance of the fluid K, the void ratio e and the specific weight of the fluid γ_s. Gu *et al.* (2003)[37] described the evolution of K and e as a function of the deformation applied to agarose gels (detailed description on Appendix I). The compression step was run using the SOILS analysis in Abaqus, which accounts for the pore pressure response and permeability. Because large deformation was used on our tests, the nonlinear geometric option (NLGEOM) was applied. To avoid discontinuities on the step resolution, the maximum pore pressure change per increment was set to 10 Pa.

Regarding boundary conditions, the fluid pore pressure p^f was set to zero on the cylindrical periphery (right side) to allow the fluid flow in the radial direction. Furthermore, to simulate the rigid and impermeable platen, all displacements and rotations were constrained using an encastre boundary condition on the bottom platen. The contact with the platens compressing the hydrogels was assumed to be perfectly lubricated and defined as a frictionless contact. Two different predefined fields were created on the initial step. The first one was used to initialize the internal state variables, which were set to zero. The second one defined the initial void ratio of the sample and was set to e_0 (see Appendix I).

Nonlinear analysis was performed using the Newton-Raphson algorithm. The hydrogel sample was modeled by the coupled pore-fluid/stress CAX8P elements, 8-node quadrilateral axisymmetric elements that considers biquadratic displacement and bilinear pore pressure. By subsequent mesh refinements, the results presented here were demonstrated to be mesh-size independent.

This model was used to simulate the two different tests conducted for this study: multi-step stress-relaxation and creep. To simulate stress-relaxation, a displacement u_y was prescribed on the top platen using a tabular amplitude to match the strain previously described in Section 2.1. To simulate creep, a range of pressures P_y were prescribed to the top platen with its respective tabular amplitude as well to simulate a constant strain ratio during the compression stage. To assess the role of poromechanics alone, we first assumed that the solid skeleton behaves as a compressible Neo-Hookean hyperelastic solid. In this context, the sample deformation is measured by the deformation gradient $\boldsymbol{F}(t) = d\boldsymbol{x}(t)/d\boldsymbol{X}$ which represents the linear mapping between the position vector $\boldsymbol{X}$ of a material point in the reference configuration and its position $\boldsymbol{x}(t)$ in the current configuration (Figure 4). In the case of unconfined compression, this tensor takes the simple form $\boldsymbol{F}(t) = diag[\lambda,\lambda_l, \lambda_l]$, where $0 < \lambda \leq 1$ is the length ratio along the vertical direction and $\lambda_l \geq 1$ represents the lateral length ratio.

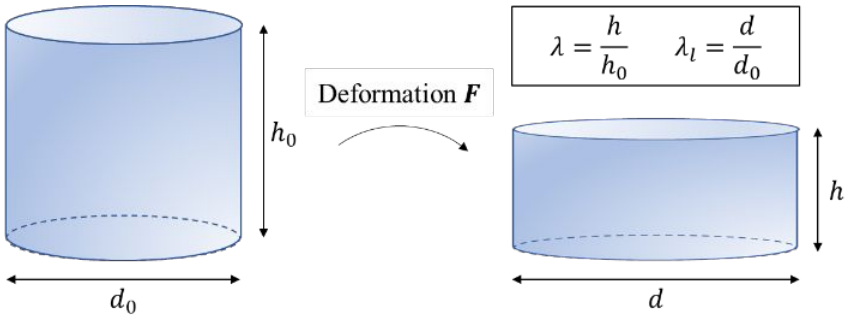

Figure 4. Conceptual diagram of deformation gradient tensor $\boldsymbol{F}$, the length ratio along the axial direction λ and the lateral length ratio λ_l.

The material strain is defined by the Finger deformation tensor (or left Cauchy-Green deformation tensor) $\boldsymbol{b} = \boldsymbol{F}\boldsymbol{F}^T$, which may further be decomposed into a volumetric component $J_e = \sqrt{\det \boldsymbol{b}}$ and an isochoric component $\overline{\boldsymbol{b}} = J_e^{-\frac{2}{3}}\boldsymbol{b}$. With these definitions, the strain energy density (per reference volume) of our compressible Neo-Hookean model is provided by

$$\psi = c_{10}(\mathrm{tr}\,\overline{\boldsymbol{b}} - 3) + \frac{1}{D_1}(J_e - 1)^2 \qquad 2$$

The material constant c_{10} and D_1 can further be written in terms of the more familiar elastic modulus E_s and the Poisson's ratio ν_s of the solid network respectively:

$$c_{10} = \frac{E_s}{4(1+\nu_s)} \; and \; D_1 = \frac{6(1-2\nu_s)}{E_s} \qquad 2.b$$

The true (Cauchy) stress tensor can then be derived as:

$$\boldsymbol{\sigma} = \frac{2}{J_e}\boldsymbol{b}\frac{\partial \psi}{\partial \boldsymbol{b}} = \frac{2}{J_e}c_{10}\mathrm{Dev}\,\overline{\boldsymbol{b}} + \frac{2}{D_1}(J_e - 1)\boldsymbol{I} \qquad 3$$

where the deviatoric part of $\overline{\boldsymbol{b}}$ is given by $\mathrm{Dev}(\overline{\boldsymbol{b}}) = \left(\overline{\boldsymbol{b}} - \frac{\mathrm{tr}\,\overline{\boldsymbol{b}}}{3}\boldsymbol{I}\right)$. The Poisson's ratio ν_s for the solid network was experimentally determined by imaging and measuring dimensions of each sample before compression and 50 minutes after the load was applied. Poisson's ratio was found to be $\nu_s = 0.17$, which is in good agreement with previous studies[19,38]. The Poisson's ratio in this study was assumed to remain constant during testing.

To obtain the elastic modulus E_s of the network, an optimization algorithm was developed to directly compare the contact force from modeling results and the experimental data (see Appendix III). In this case, contact force obtained from first compression stage ($\epsilon = 0.05$) on the multi-step stress-relaxation on 5% w/w agarose gels was used. E_s is set to be equal to 0.81 MPa.

Numerical simulations together with experimental findings indicate that poromechanics plays only a minor role stress relaxation. From simulations, we can state fluid transport occurred within the first 2000 s (~ 35 min) (Figure 5.C and 5.D); then stress remained constant until the end of the simulation.

2.5. Experimental confirmation of poromechanical effects

We next sought to experimentally confirm our finding that poroelasticity did not dominate the behavior of agarose under the parameters applied in our computational analysis. Mass loss from samples was performed to experimentally confirm the minor role of energy-dissipation from poromechanics (Table 1). The amount of water released increased with increasing sample diameter due to the higher water content in the initial state. In relative terms, Table 1 shows that the amount of water loss remained constant with respect the initial gel mass $\left(\|\Delta\overline{m}\| = \left\|\frac{\Delta m}{m_1}\right\| = 10.1\%\right)$, independently of sample size.

d [mm]	m_1 [g]	Δm [g]
8.66	0.57 ± 0.022	- 0.05 ± 0.028 (-9.34%)
12	1.32 ± 0.084	- 0.14 ± 0.033 (-10.7%)
16	3.43 ± 0.17	- 0.35 ± 0.069 (-10.3%)

Table 1. The initial mass of the agarose gels is shown as m_1. Mass variation on gels due to the water mass loss, is reported as Δm and is calculated as $\Delta m = m_2 - m_1$, where m_1 initial mass of the sample and m_2 is the mass measured after the experimental test.

The effect of water loss was also assessed through the diametrical contraction of the sample during stress-relaxation testing (Figure 5.E). When compression is held, pressurized pore fluid slowly leaves the system in the radial direction of the sample while pores within it collapse reducing its volume. When diametrical contraction stops due to this phenomenon, it can be understood as the end of the poromechanics contribution to the energy dissipation. The experimental data recorded dissipated energy after the poroelastic model (Section 2.4) plateaued which increased the difference between the equilibrium forces. Based on this observation, the purely poroelastic computational model was insufficient to explain the behavior of agarose in response to unconfined compression observed during the relaxation stage. However, for lower agarose concentrations, agarose network may become poorly crosslinked (i.e., near the percolation threshold). Arbabi and Sahimi (1993) concluded that for networks with low connectivity, the capabilities of continuum models may be limited since the affine deformation assumption can no longer be applied[39]. Due to the network's decreased cross-link density, viscoelasticity might not be as dominant in that situation as for higher agarose concentration.

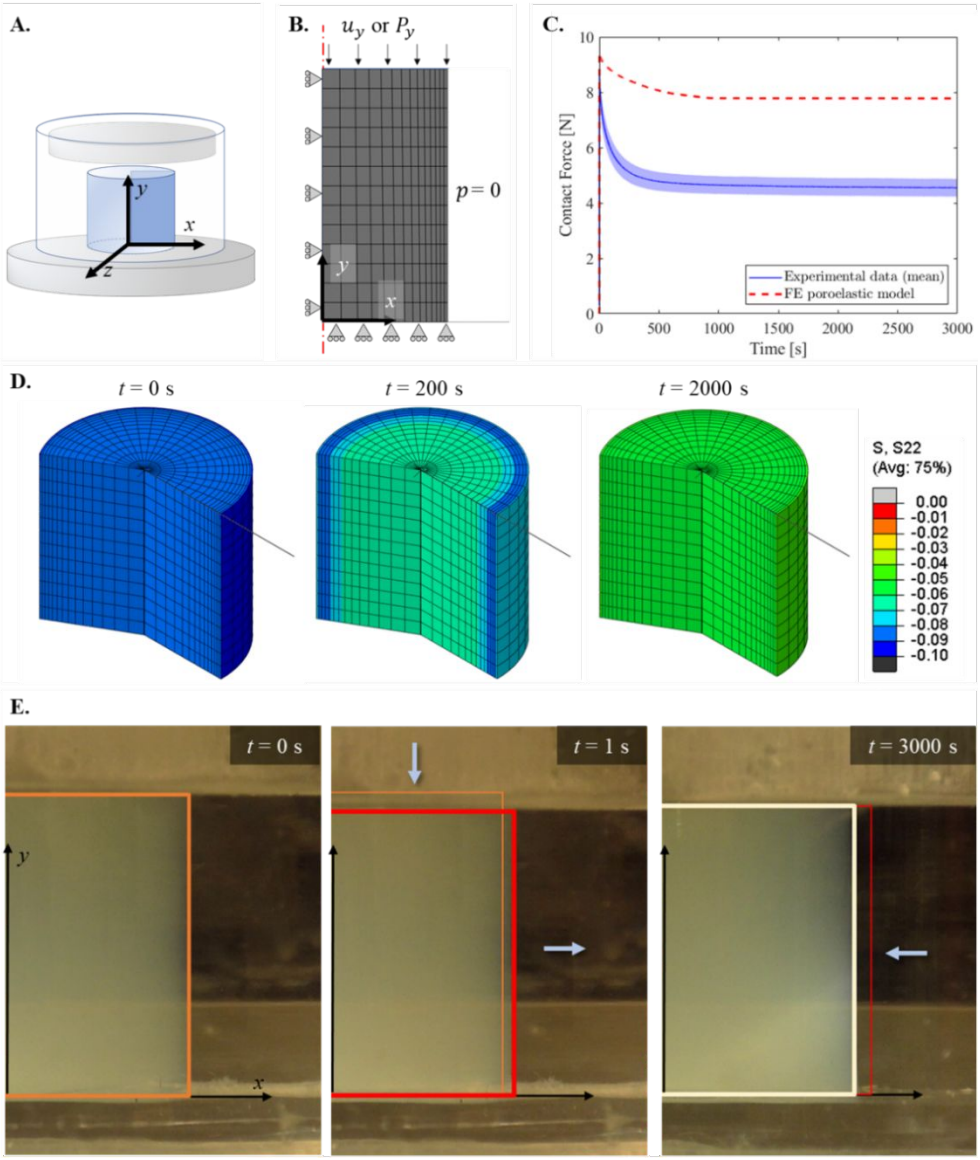

Figure 5. **A**. Schematic of unconfined compression of a cylindrical agarose sample. **B**. The computational domain along with the mesh and the boundary conditions implemented. In the boundary conditions, p is the pore pressure and u_y the axial displacement applied when multi-step stress-relaxation is simulated or P_y the axial pressure applied when creep is

simulated. **C**. Abaqus poroelastic model prediction results (red dashed line) for stress-relaxation test for 16 mm, 5% w/w agarose gels versus experimental data (solid blue line -average value from the different samples tested- and a blue region -average ± standard deviation). **D.** Three different time frames (from top to bottom, 1 s, 200 s and 2000 s) are plotted to show the stress distribution in the axial direction. It is possible to observe how the poroelastic effect generates a gradient on the stress distribution. After the fluid transport ceased, the stress field became uniform and the solid network was the only part of the system dissipating energy. **E**. Photographs were taken during stress-relaxation test on 16 mm, 5% w/w agarose gels to experimentally quantify the Poisson's ratio of the solid skeleton and determine the order of magnitude of the characteristic time corresponding to the fluid leaving the system. The compression stage had a duration of 1 s where the gel expanded laterally. The relaxation process was recorded while the gel contracted laterally due to the fluid leaving the system. The gel stopped shrinking at 3000 s after the compression stage.

3. AGAROSE AS A NONLINEAR TRANSIENT NETWORK

The time-dependent inelastic response of agarose samples in this study was dominated by viscoelasticity, rather than poroelasticity. In the literature, the mechanical behavior of agarose have generally been characterized by an elastic and a time-dependent or viscous component using phenomenological viscoelastic models[21–23] (i.e., the simplest being the Maxwell model). These models however remain mostly empirical, which motivates the current work as an attempt to build a connection between the gel's network topology and its mechanical response.

3.3. Preliminaries: the transient network theory

Let us start by introducing a theoretical framework to describe the nonlinear viscoelasticity of polymer networks, known as the transient network theory (TNT)[27,40]. Due to the presence of physical crosslinks in agarose structure[41], the network is assumed to be dynamic, wherein the polymer chains associate and dissociate over time.

The polymer is thus idealized as a network of polymer strands with the end-to-end vector $\boldsymbol{r}$ which represents as the segment between two nodes or crosslinks. For convenience, we introduce the normalized end-to-end vector $\boldsymbol{\lambda} = \frac{\boldsymbol{r}}{r_0}$ where r_0 is the natural (force-free) length of a strand. In the TNT, a statistical description of the network is provided by the density c of connected strands and the so-called strand conformation tensor, with indices μ_{ij} given by

$$\boldsymbol{\mu}(t) = 3\langle \boldsymbol{\lambda} \otimes \boldsymbol{\lambda} \rangle \tag{4}$$

where the operation $\langle\ \rangle$ denotes the average chain deformation of all connected strand within a representative volume element. If the network is initially isotropic, it verifies $\boldsymbol{\mu}(0) = \boldsymbol{I}$. Under the affine deformation assumption[42], the change in stretch of a connected strand verifies $\dot{\boldsymbol{\lambda}} = \boldsymbol{L} \cdot \boldsymbol{\lambda}$ where $\boldsymbol{L}$ is the velocity gradient $\boldsymbol{L} = \dot{\boldsymbol{F}}\boldsymbol{F}^{-1}$. Therefore, it is possible to construct an evolution equation for the strand conformation tensor if the rates of chain association and dissociation previously described are known[27].

$$\dot{\boldsymbol{\mu}} = \boldsymbol{L}\boldsymbol{\mu} + \boldsymbol{\mu}\boldsymbol{L}^T - k_d\boldsymbol{\mu} + k_a\frac{C-c}{c}\boldsymbol{I} \tag{5}$$

where C is the total number of strands per unit volume the network (including both connected and dangling contributions), and k_a and k_d are the kinetic rates describing polymer chains association and dissociation, respectively. For simplicity, we assume there is a perfect bond exchange within the network, meaning each detachment event is immediately followed by an attachment event[43]. We also consider the case of incompressible plastic flow. The evolution equation becomes the following[44]:

$$\dot{\boldsymbol{\mu}} = \boldsymbol{L}\boldsymbol{\mu} + \boldsymbol{\mu}\boldsymbol{L}^T - k_d\left(\boldsymbol{\mu} - \frac{3}{\mathrm{tr}\,\boldsymbol{\mu}^{-1}}\boldsymbol{I}\right) \tag{6}$$

From this relation, it is straightforward to show that for a covalently cross-linked network ($k_d = 0$) the conformation tensor $\boldsymbol{\mu}$ is equivalent to the left Cauchy-Green tensor $\boldsymbol{b}$, i.e. $\boldsymbol{\mu} = \boldsymbol{b} = \boldsymbol{F}\boldsymbol{F}^T$[27]. Similarly to Equation 3, the true stress tensor can then be derived in terms of the conformation tensor as[40,45]

$$\boldsymbol{\sigma} = \frac{2}{J_e}\boldsymbol{\mu}\frac{\partial \psi}{\partial \boldsymbol{\mu}} = \frac{2}{J_e}c_{10}\mathrm{Dev}\,\bar{\boldsymbol{\mu}} + \frac{2}{D_1}(J_e - 1)\boldsymbol{I} \qquad 7$$

where the deviatoric part of $\bar{\boldsymbol{\mu}}$ is given by $\mathrm{Dev}\,\bar{\boldsymbol{\mu}} = \bar{\boldsymbol{\mu}} - \frac{\mathrm{tr}\,\bar{\boldsymbol{\mu}}}{3}\boldsymbol{I}$. Material constants c_{10} and D_1 were defined in Equation 2b. This model describes a material that displays a linear elastic response (through its Neo-Hookean form), and a linear viscoelastic response (since the rate constant k_d remains constant). Note that this model may however still capture nonlinear geometrical effects since it is valid for large strains. The viscoelasticity of agarose was however observed to be quite nonlinear, which motivates the development of a more physical model regarding the relaxation mechanisms occurring within the polymer structure. Such a theoretical improvement must therefore involve a rate constant k_d that changes with stress as previously discussed in Hui *et al*. (2021)[46].

3.4. *Nonlinear bond dynamics of agarose-based gels*

Hydrogen bonding not only governs the self-gelation of agarose gels, but it also facilitates the complex dynamics of the resulting network. Hydrogen-bonding side groups found in agarose facilitate the formation of transient supramolecular structures with viscoelastic responses[47]. It is theorized that there are two main microstructural features that contributes to agarose viscoelastic behavior. First, aligned agarose molecules that form double helices have a limited mobility in comparison with single agarose molecules. This dynamic gel structure has been proposed to occur at short relaxation times. In contrast, agarose molecules present in clusters that are not aligned with each other can dissipate energy much more easily as they slide over adjacent molecules, corresponding to a fluid-like behavior[17]. This behavior is illustrated in Figure 6.

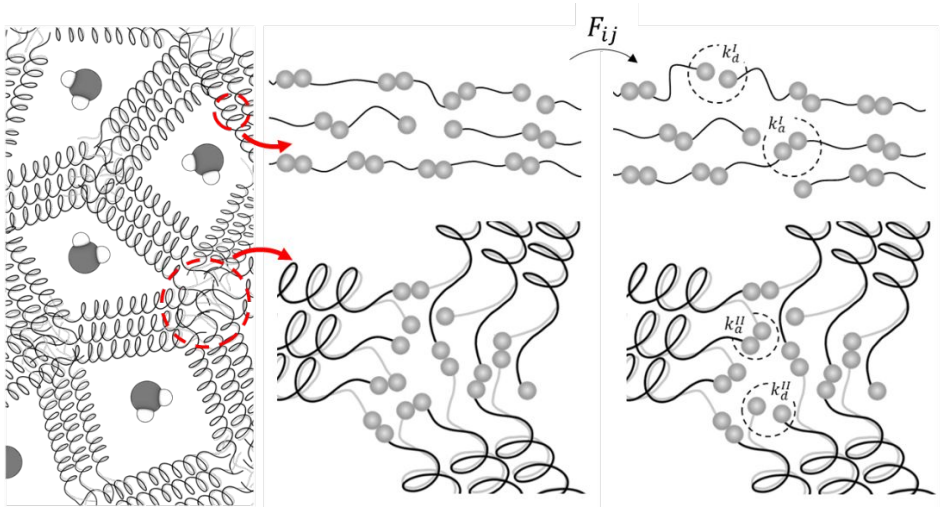

Figure 6. Schematic of the short relaxation time on agarose corresponding to the fast bond dynamics (k_d^I and k_a^I) of the strands aligned on the double helices (top) and of the long relaxation times associated to the slow bond dynamics (k_d^{II} and k_a^{II}) where agarose molecules presented in the suprafibers clusters can dissipate energy much more easily as the they slide over adjacent molecules (bottom).

Our experimental results suggest that agarose networks have two different dissipation mechanisms when subjected to an external stress[48]. To construct a model for this network, we first assume each mechanism has its own characteristic dissociation rate such that global the kinetic rate k_d is decomposed as:

$$k_d = k_d^I + k_d^{II} \qquad 8$$

Here k_d^I is the fast dissociation rate associated to the rearrangement of the strands aligned forming the double helix structure and k_d^{II} is the slow dissociation rate associated with the bond exchange in the suprafiber junctions. A closer look at experimental data suggests that the transition between the above two relaxation mechanisms is smooth and a function of the overall stress-state of the specimen. The fast rates k_d^I is assumed to change with the level of stress, or alternatively, the level

of elastic deformation while the slow constant k_d^{II} is assumed to remain constant over the time scale of the experiments. For simplicity, we follow classical plasticity theory and assume that volumetric deformation does not affect inelastic flow[49]. This model assumption can easily be relaxed in future implementation of the model if further experiments show it to be inaccurate. We can therefore define a scalar measure of the isochoric elastic deformation via an "effective elastic strain" defined as:

$$\bar{\mu} = \sqrt{\frac{3}{2}\mathrm{Dev}(\bar{\boldsymbol{\mu}}):\mathrm{Dev}(\bar{\boldsymbol{\mu}})}\ ,$$

such that the fast relaxation rate is defined with a generic function $f(\bar{\mu})$ in the form:

$$k_d^I = k_{d0}^I f(\bar{\mu}) \qquad 9$$

The scalar function $f(\bar{\mu})$ need to be derived based on the experimental data collected. Observation of the creep test data suggests that agarose does not show significant creep for $\bar{\mu} < \beta$. However, for values of $\bar{\mu} > \beta$ (Figure 8.A), creep suddenly accelerates and the function k_d^I maybe assumed to follow the relation $k_d^I = k_d^0 \exp(\gamma\bar{\mu})$. This exponential relation is in line with the theoretical model presented by Eyring experiencing force-dependent bond dynamics[50–52]. Combining this statement along with the observation made from multi-step stress relaxation tests, the evolution of k_d is hypothesized to follow a generalized logistic function with the following expression:

$$f(\bar{\mu}) = \frac{e^{\gamma\bar{\mu}}}{1 + e^{-\alpha(\bar{\mu} - \beta)}} \qquad 10$$

where β represents the elastic strain trigger for bond dynamics, and γ is defined as the stress-sensitivity of bond dynamics. In addition, as depicted in Figure 7, coefficient α describes the sharpness of the transition between the two energy dissipation mechanisms; if $\alpha \to \infty$, the transition is very steep and converges to a step function while $\alpha \to 0$ indicates a very smooth transition showing a perfect coupling between the two relaxation mechanisms during the whole relaxation process. The coefficient β follows the evolution of the equilibrium or plateau stress σ_p point seen in Figure 2.C-D-E.

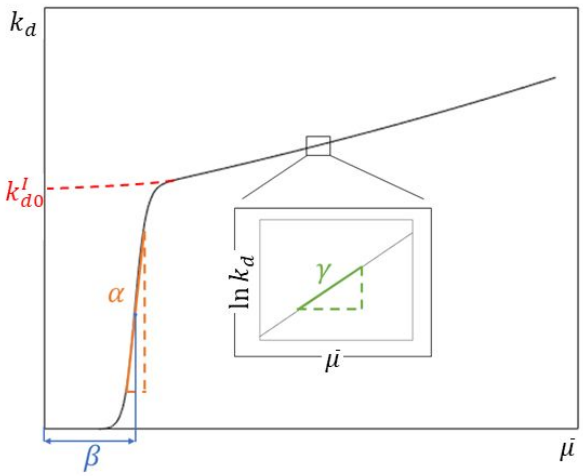

Figure 7. Physical interpretation of the fitting parameters used to describe the bond dynamic evolution: α is the bond dynamics transition steepness, β is the elastic strain trigger for bond dynamics, γ is the stress-sensitivity of bond dynamics and k_{d0}^I is the spontaneous dissociation once the stress threshold is triggered.

3.5. Implementation and experimental validation

The above viscoelastic model was implemented into a UMAT Abaqus subroutine requiring the calculation of the Cauchy stress $\boldsymbol{\sigma}(\bar{\boldsymbol{\mu}})$ and tangent stiffness matrix $\boldsymbol{C}(\bar{\boldsymbol{\mu}})$. Using expressions provided in Appendix II, Equation **Error! Reference**

source not found. was invoked to enforce the evolution of the conformation tensor as a function of the dissociation ratio of the network. To summarize, the material behavior of the hydrogel depends on two physical processes that are captured by (a) a UMAT subroutine for the solid matrix based on the TNT to control the viscoelasticity of the skeleton, and (b) an Abaqus material library to describe the poroelasticity due to the pore fluid flow of the solvent.

Running the optimization procedure detailed on Appendix III on the creep data and, separately, on the multi-step stress-relaxation data, it was further possible to accurate calculate model parameters α, β, γ and k_{d0}^{I}. Using data from the creep test, it was further possible to accurate calculate the exponential evolution of k_d^I where, independently of the concentration of agarose used, we found mean values of $k_{d0}^{I} = 0.001164$ 1/s and $\gamma = 2.412$ (Figure 8.A); this expression accurately predicts the values for k_d^I when $\bar{\mu} < \beta$.

Using data from the multi-step stress-relaxation and our optimization algorithm, the parameters α and β were empirically fitted for various agarose composition and applied strain (see Figure 8.B). Different initial guess values were used as an input to the optimization algorithm.

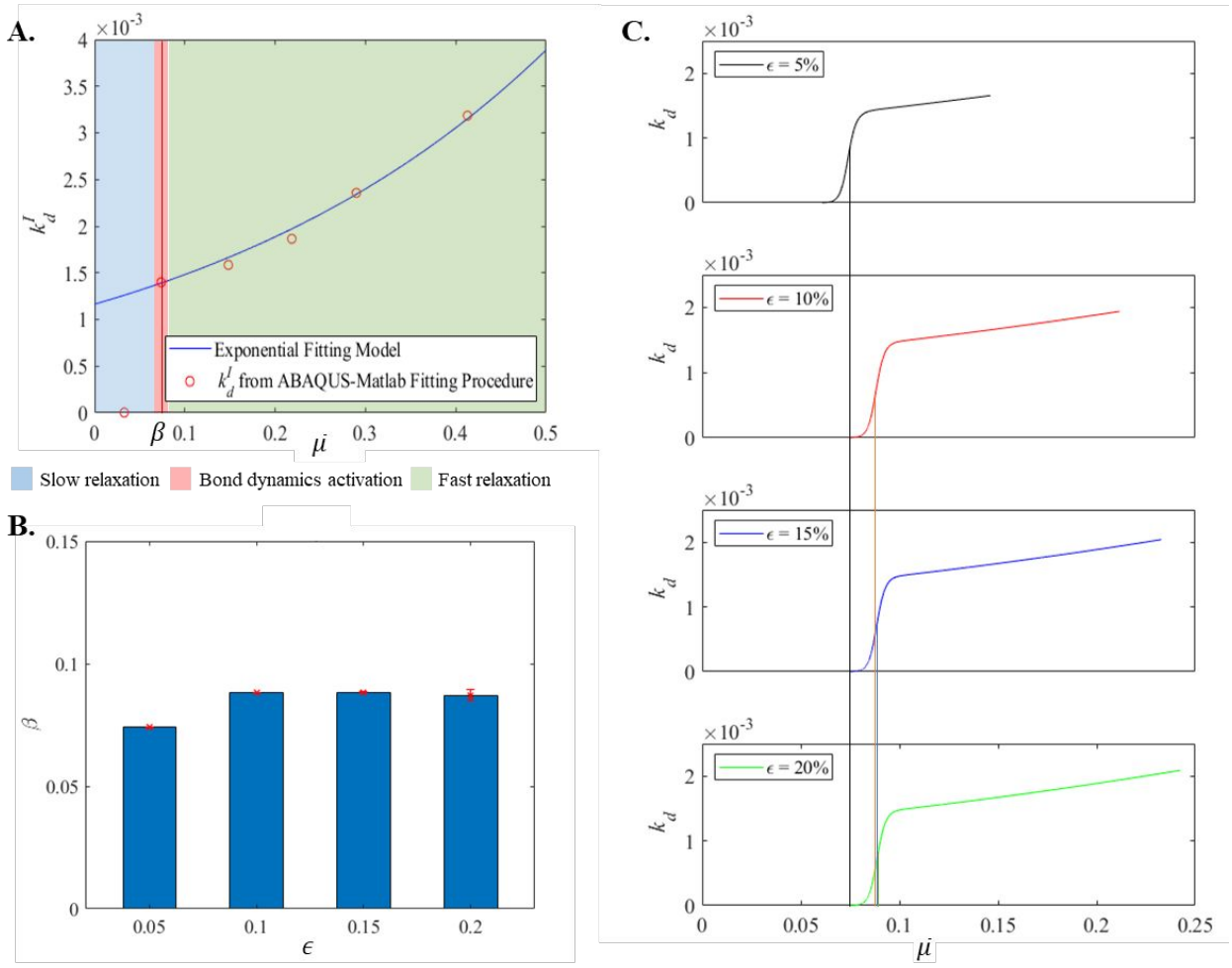

Figure 8. A. Dissociation rate exponential evolution obtained from the optimization algorithm ran on the experimental creep test data on 12 mm, 5% w/w agarose gels. Graphing the results shows three different zones: slow relaxation domain (blue zone), fast relaxation domain (green zone) and the elastic strain trigger, β, zone for bond dynamic activation (red zone). **B.** For $\alpha = 500$, average values for the different agarose concentrations of the evolution of the elastic strain trigger for bond dynamics β at different applied strains during the multi-step unconfined compression test. **C.** For 10% w/w agarose, evolution of the bond exchange rate as a function of $\bar{\mu}$. Vertical lines represent the values for the bond dynamic trigger parameter β.

This data suggests that while the sharpness of the bond dynamics transition remains constant across the multiple compression steps, the elastic strain trigger, β, changes its values to account for the stress plateauing during the whole test (Figure 8.B). Therefore, β follows the plateau point evolution. For the 5% w/w case, β decreases for the last stress-relaxation step. This agrees with the experimental data of Figure 2.C where the plateau stress σ_p measured in the last compression step (20% strain), is below the one measured for 15% strain. For 7.5% and 10% w/w agarose, the same fitting parameter were used for strains > 5%. In these cases, the sharpness of the transition remains constant, but β slightly increases its value at each deformation step. Taken together, these results suggest that the evolution of bond dynamics is independent of agarose concentration.

The dissociation constant k_d^{II} of the cluster was obtained using the optimization algorithm. We found that k_d^{II} is generally insensitive to stress and agarose concentration which confirms it can be kept constant. We estimated the mean rate constant as $k_d^{II} =$ 2.76E-6 1/s (i.e., $k_d^{II} \ll k_d^I$). In the remainder of our analysis (i.e., that concentrates on shorter time scales), this rate can therefore be neglected compared to k_d^I, and a general evolution equation for the general kinetic rate is $k_d \approx k_d^I = k_{d0}^I f(\bar{\mu})$. Therefore, as an input for the UMAT subroutine five parameters are necessary to describe the solid matrix behavior: the elastic modulus E_s of the solid network, Poisson's ratio ν_s of the solid matrix and the empirical variables α, β, γ and k_{d0}^I.

Figure 9. demonstrates agreement between the poroviscoelastic model and the time-dependent mechanical response of agarose gels during experimental creep (5% w/w agarose) and multi-step stress relaxation (5, 7.5, 10% w/w agarose) testing. Figure 8.B. and Figure 9.B-D. also verify the evolution of bond exchange rate behaves independently of agarose concentration. Inset plot in panel A in Figure 9 corroborates the model captures the three creep regimes (primary, secondary and tertiary creep) in experimental data. Insets plots in panels B-D in Figure 9, shows the model captures the short-term experimental response of agarose gels. We notice energy is dissipated faster on the experimental data than on the computational model for short time scales, yet such difference does not affect the equilibrium response.

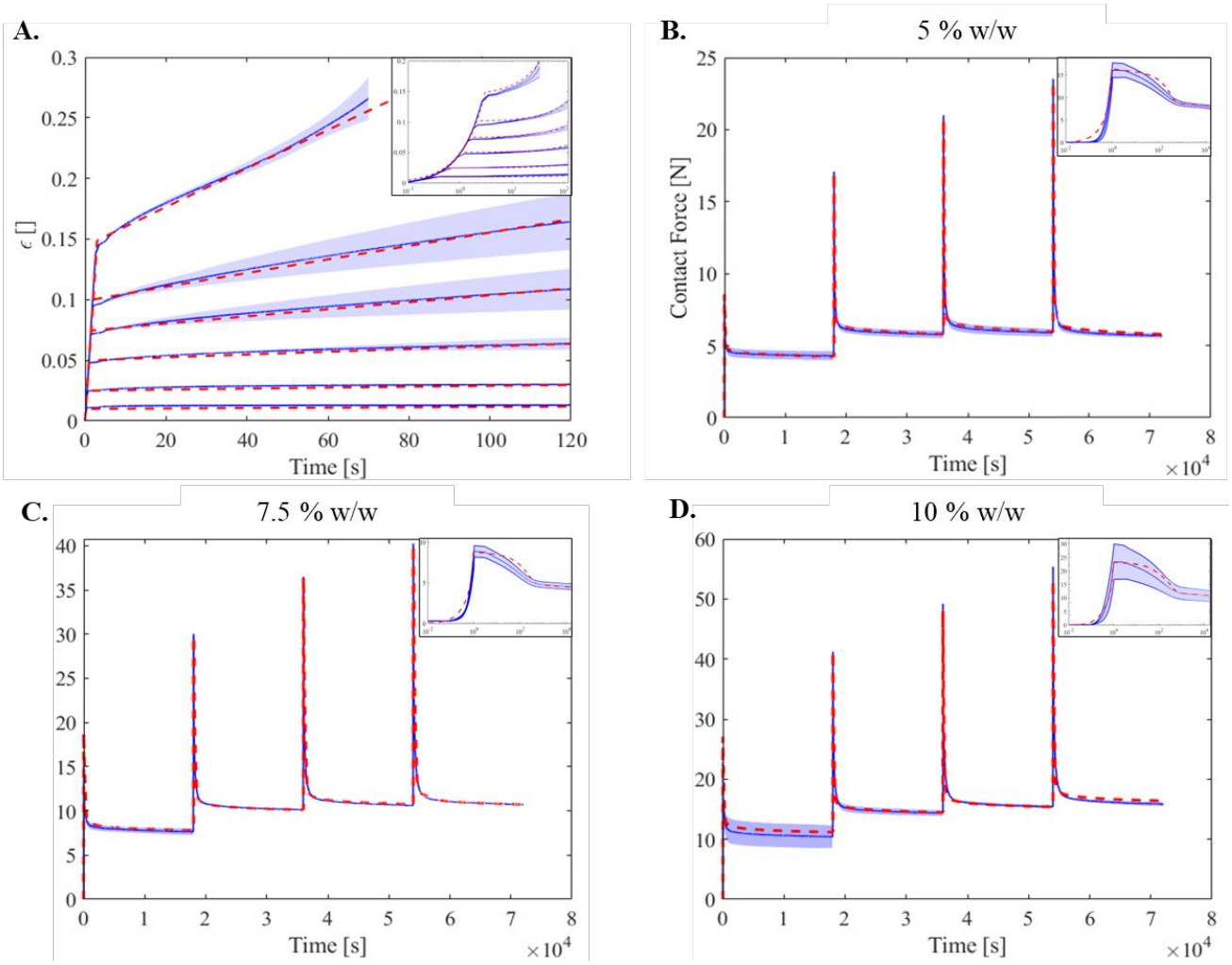

Figure 9. Comparison of the prediction from finite element predictions against experimental measurements for tested samples. Abaqus simulation results are represented by red dotted line, and experimental results are reported as a blue solid line (mean values from experimental tests) and blue region (average ± standard deviation). **A.** Results of creep test for 12mm, 5% w/w agarose gels. The inset in **A**. shows creep test results in a semilogarithmic scale along the x-axis. **B.**, **C.**, and **D**. Results of multi-step stress relaxation tests for 5%, 7.5% and 10% w/w agarose gels respectively. The inset in **B-D**. shows the stress evolution for the first loading and relaxation step in a semilogarithmic scale along the x-axis.

4. DISCUSSION

We developed a physically based model to describe and predict the time-dependent behavior of agarose networks under unconfined compression. Unlike prior phenomenological and continuum models describing viscoelasticity, our approach considers the time-dependent evolution of the stress-dependent variables that result from bond-exchange within the polymer network. This work provides a reinterpretation of agarose network viscoelastic behavior using the transient network theory (TNT). Using the characterization of the two main microstructural features that contribute to agarose viscoelastic behavior, which are based on dissociation and reassociation of molecular bonds within agarose, we demonstrated that the network deforms over time through non-linear force-dependent evolution of bond dynamics.

Agarose gels are formed from hydrogen (e.g., dynamic) bonds that re-attach after disengaging which imparts gels with viscoelastic behavior. Here, viscoelasticity was assumed to follow the two main characteristic microstructures of the gel network described by Labropoulos *et al.* (2001)[48]. Assuming perfect bond exchange, we hypothesized that the overall dissociation rate (k_d) results from a linear combination of the dissociation rate corresponding to double helices forming between aligned agarose molecules (k_d^I) and the dissociation rate of the agarose molecules present in the clusters (k_d^{II}). Due to the degree of mobility of the agarose, these factors are responsible for the short ($1/k_d^I$) and longer ($1/k_d^{II}$) relaxation times,

respectively. The present work incorporated these topologically based phenomena into a mathematical model, the TNT, thus enabling a novel quantitative understanding of the relationships between molecular physics and overall mechanical response. This methodology may be extrapolated to other biopolymer networks with similar topologies (i.e., collagen and fibrin networks) to predict their emerging material response as a function of bond kinetics.

The fast bond dynamics of agarose network (k_d^l) associated to the aligned agarose molecules exhibited significant force-sensitive dynamics. In the creep test, we observed that the magnitude of the applied stress had the effect of weakening the solid-like behavior of the network associated to the fast energy dissipation mechanism. We interpreted this behavior as a reorientation of the agarose network along the direction of applied compression which is a particular property of semiflexible networks. Our model suggested an exponential force-dependent response of the fast dissociation rate, which agrees with Eyring's theory[50]. Capturing this phenomenon revealed a novel insight in agarose viscoelastic properties: i.e., the lifetime of a bond depends on the force applied to that bond.

We further demonstrated the non-linear viscoelasticity of agarose hydrogels throughout the implementation of a non-constant dissociation rate. In our study, the nonlinear viscoelasticity could be observed by a stress-plateauing effect during a multi-step stress relaxation test. In particular, the equilibrium stress at the end of the relaxation phase plateaued and reached the same value independent of the applied deformation. We developed a master equation to describe the bond exchange (Equation **Error! Reference source not found.**) based on physics-based parameters such as the elastic strain trigger for bond dynamics and the stress-sensitivity of the bond rate. The same behavior was observed in multi-step stress relaxation testing (with a 30 minute relaxation period) reported by Roberts *et al.* (2011)[12] in their comparative study of the viscoelastic mechanical behavior of agarose and poly(ethylene glycol) hydrogels. Because of the relatively short time used between step strains in their study, the stress did not plateau as reported herein; however, the trends in both studies are consistent.

Following the stability of adhesion clusters model presented by Erdmann and Schwarz (2004)[53], we hypothesized that the clusters formed by several suprafibers within agarose networks increased the number of connected bonds during the deformation process (Figure 10). Cluster adhesion was presented in previous literature as a likely mechanism for stress relaxation in biopolymers[54–56]. For example, Prechtel *et al.* (2002) studied cluster dissociation under a linear ramp of force and described the strength of the adhesion of living cells to model membranes[57]. Briefly, Erdmann and Schwarz postulated a detailed theoretical analysis of the stochastic dynamics of a cluster of parallel bonds under shared constant loading and with rebinding. The adjacent agarose molecules that are not part of the cluster in a stress-free configuration may be available to later form new crosslinks with the initial components of the cluster. This theory provides a mechanism for increasing cluster size and a strengthening of the network. Following this theory, we found the elastic modulus of agarose slightly increased with elastic deformation which indicated a mild strain stiffening effect during sustained compression (Appendix IV). Future investigations should further evaluate our hypothesis for a potential relationship between the elastic strain trigger for bond dynamics and cluster size and should also consider other possible competing mechanisms such a viscoelastic elongation of the network chains[58,59].

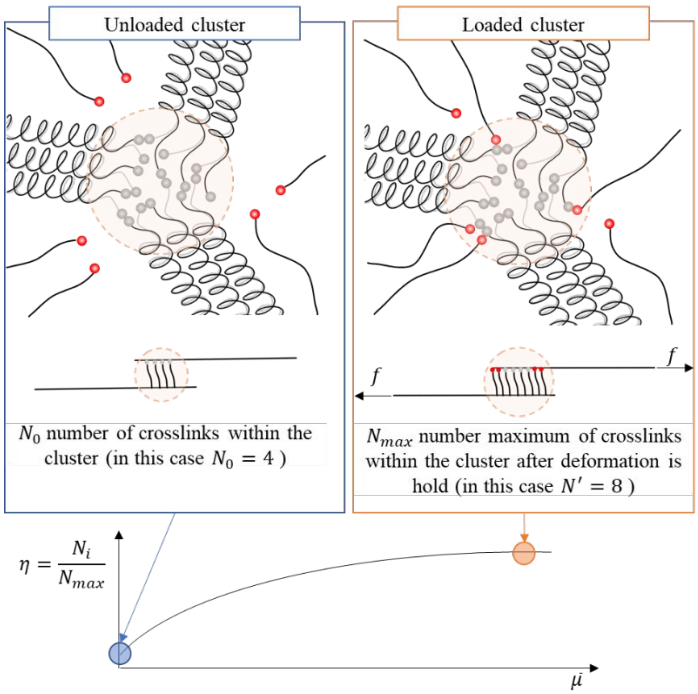

Figure 10. Schematic representation of the number of bonds N_i within a cluster in agarose network before and after a stress field is applied. Unbonded agarose molecules join the cluster as the external force increases. Variable η is defined to represent the cluster bond saturation plateauing after the force f held by the cluster exceed a certain threshold value.

Poromechanical effects in agarose did not significantly contribute to energy dissipation during stress-relaxation. These results followed the well-studied poroelastic material behavior of agarose in the literature[37,60–64]. We observed that the influence of time-dependent fluid displacement on the gel's response to be small. However, we still incorporated it in our analysis for the following reasons. First, we observed a reduction of the initial hydrogel mass during long-duration compression tests; this effect can only be captured by poromechanics. Second, the incorporation of fluid transport during loading allowed for a more general formulation that may explain coupling of poromechanics with network relaxation; this point can be used to better understand poroviscoelastic behavior of agarose gels. Demonstrating the minor role of poromechanics in agarose supported the use of the TNT to control and predict the macroscopical time-dependent response of physically crosslinked gels.

Unlike prior applications of the TNT in 2D[40], our study demonstrated the application of the TNT into a commercial FEA software. This approach will allow for future 3D modeling of complex polymer behavior (i.e., crack propagation or cavity generation[65]) using an underlying mechanism-based material model. We also demonstrated an initial step that will enable a continuum approach of the TNT to be applied to more complex geometries (i.e., 3D printed hydrogels) than the cylindrical geometry presented in this study. The computational implementation of the TNT into a commercial FEA package, combined with experimental testing, allowed us to assess the influence of poroelastic and viscoelastic effects in the overall macroscopic response of agarose to time-dependent experiments.

Finally, we emphasize that the model presented in this study can be used to provide control guidance on the material design in numerous applications, many of which are applicable to bioengineering, that necessitate the use of agarose and similar gels. The TNT model also offers the possibility to design and fabricate gels based on their bond dynamic to obtain a specific time-sensitive behavior. One important future effort is to extend the current model to different biopolymers with similar network topology and to determine if the TNT can be universally applied to describe behavior of similar biopolymers. Finally, our work may also support a variety of tissue engineering applications and provide physical insights to understand the force-dependent viscoelastic behavior. For instance, understanding how the yielding behavior of agarose gels may be crucial for a wide range of biomedical applications where gels are subjected to loads over long periods of times.

ACKNOWLEDGMENT

VLF acknowledges funding support from the National Institutes of Health Award numbers 1R33HD090696 and 1R01AR069060. FJV gratefully acknowledges the support of the National Science Foundation under Award No. 1761918. The content is solely the responsibility of the authors and does not necessarily represent the official views of the National Science Foundation.

CONFLICT OF INTEREST

There are no conflicts of interest.

APPENDIX I: INTRINSIC PERMEABILITY AND VOID RATIO EVOLUTION IN AGAROSE GELS

The intrinsic permeability κ for agarose gels was defined using the evolutions equations described by Gu *et al.* (2003)[37].

$$\kappa = \kappa_0\left(\frac{J_e-\phi_0}{1-\phi_0}\right)^n, \phi = \frac{\phi_0}{J_e} \quad (11)$$

Therefore, in this study, the intrinsic permeability κ and the solid volume fraction ϕ were assumed to be a function of the macroscopic deformation applied on the gel, in this case using the Jacobian J_e of the elastic deformation gradient tensor $\boldsymbol{F_e}$. The initial permeability was defined as $\kappa_0 = p_1\left(\frac{1-\phi_0}{\phi_0}\right)^{p_2}$ where p_1 and p_2 were fitting parameters. Here, the initial solid volume fraction ϕ_0 was obtained using the relationship established by Pluen *et al.* (1999)[60]; $\phi_0 = \frac{1}{\rho_{agarose}\omega_{agarose}}c_o$ where c_o is the agarose concentration, $\rho_{agarose}$ = 1.64 g/ml is the dry agarose density[61] and $\omega_{agarose}$ = 0.625 is the mass fraction of agarose in a fiber[62].

The initial hydraulic conductance K was defined as $K = \frac{\gamma_s}{\mu}\kappa$ where μ is the dynamic viscosity of the fluid and γ_s is the specific weight of the fluid. Since the fluid was a PBS solution, $\mu =$ 1E-9 N·s/mm^2 and γ_s = 9.81E-06 N/mm^3. Once ϕ was calculated and assuming the porosity $\theta = 1-\phi$, the void ratio was defined as $e_0 = \frac{\theta_0}{1-\theta_0} = \frac{J_e}{\phi_0} - 1$. Values were summarized in Table 2 and assumed to remain constant during the whole deformation process.

c_o[%]	ϕ_0[%]	e_0	κ_0 [mm^2]	K_0 [mm/s]
5	4.88	19.5	2.32E-11	2.56E-07
7.5	7.32	12.67	1.22E-11	1.22E-07
10	9.76	9.25	7.75E-12	7.60E-08

Table 2. Parameters used to describe poromechanics for each agarose composition used in the study.

APPENDIX II: CAUCHY STRESS AND TANGENT STIFFNESS MATRIX DERIVATION

To derive the required expressions for the implementation of the TNT into Abaqus, we first rewrote the elastic energy as:

$$\psi = c_{10}\left(\overline{I_1} - 3\right) + \frac{1}{D_1}(J_e - 1)^2 \quad (12)$$

We here assumed elastic compressibility but inelastic incompressibility (from Equation 6). Consequently, in the remainder of our derivations, $J_e = J$. The constitutive equation for the Cauchy stress can be written directly in terms of the deformation gradient[45]:

$$\sigma_{ij} = \frac{2}{J}\mu_{ik}\frac{\partial\psi}{\partial\mu_{kj}} \tag{13}$$

Now we compute the derivatives of the invariants $\overline{I_1}$, $\overline{I_2}$ and J with respect to the conformation tensor $\boldsymbol{\mu}$ components

$$\frac{\partial\psi}{\partial\mu_{ij}} = \frac{\partial\psi}{\partial\overline{I_1}}\frac{\partial\overline{I_1}}{\partial\mu_{ij}} + \frac{\partial\psi}{\partial\overline{I_2}}\frac{\partial\overline{I_2}}{\partial\mu_{ij}} + \frac{\partial\psi}{\partial J}\frac{\partial J}{\partial\mu_{ij}}, \tag{14}$$

and obtain the stress expression

$$\sigma_{ij} = \frac{2}{J}\left[\frac{1}{\overline{J}^{\frac{2}{3}}}\left(\frac{\partial\psi}{\partial\overline{I_1}} + \overline{I_1}\frac{\partial\psi}{\partial\overline{I_2}}\right)\mu_{ij} - \frac{1}{3}\left(\overline{I_1}\frac{\partial\psi}{\partial\overline{I_1}} + 2\overline{I_2}\frac{\partial\psi}{\partial\overline{I_2}}\right)\delta_{ij} - \frac{1}{\overline{J}^{\frac{4}{3}}}\frac{\partial\psi}{\partial\overline{I_2}}\mu_{ik}\mu_{kj}\right] + \frac{\partial\psi}{\partial J}\delta_{ij} \tag{15}$$

In our case

$$\sigma_{ij} = \frac{2}{J}c_{10}\left(\overline{\mu}_{ij} - \frac{1}{3}\delta_{ij}\overline{\mu}_{kk}\right) + \frac{2}{D_1}(J-1)\delta_{ij} \tag{16}$$

To obtain the tangent stiffness matrix we first need to define virtual rate of deformation

$$\delta D_{ij} = \frac{1}{2}\left(\delta F_{im}\,F^{-1}_{\overline{m}j} + F^{-1}_{\overline{i}m}\,\delta F_{jm}\right) = \frac{1}{2}(L_{ij} + L_{ji}) \tag{17}$$

The Kirchhoff stress is

$$\tau_{ij} = J\,\sigma_{ij} \tag{18}$$

The material Jacobian derives from the variation in Kirchhoff stress.

$$\tau_{ij} = J\,C_{ijkl}\,\delta D_{kl} \tag{19}$$

then

$$C_{ijkl} = \frac{2}{J}c_{10}\left[\frac{1}{2}(\delta_{ij}\overline{\mu}_{jl} + \overline{\mu}_{ik}\delta_{jl} + \delta_{il}\overline{\mu}_{jk} + \overline{\mu}_{il}\delta_{jk}) - \frac{2}{3}\left(\delta_{ij}\overline{\mu}_{kl} + \overline{\mu}_{ij}\delta_{kl} + \frac{1}{3}\delta_{ij}\delta_{kl}\overline{\mu}_{mm}\right)\right] + \frac{2}{D_1}(J_e - 1)\delta_{ij}\delta_{kl} \tag{20}$$

$$c_{10} = \frac{E}{4(1+\nu)} \text{ and } D_1 = \frac{6(1-2\nu)}{E}$$

APPENDIX III: FITTING PROCEDURE LINKING ABAQUS AND MATLAB

To estimate the input material parameters (k_d^I, k_d^{II}, α, β, γ and k_{d0}^I) of agarose gels, an optimization procedure linking Abaqus and MATLAB (MathWorks, Natick, MA, USA) was developed. Briefly, initial guess values of the material parameters were assigned in the input file model and the Abaqus run was executed to compute the system contact force response F^{sim}. Then, the sum of root-mean-square error in the contact force was defined as

$$SE = min\sum_{i=1}^{n}\left(F_i^{test} - F_i^{sim}\right)^2 \tag{21}$$

where n is the number of iterations. Subsequently, an optimization algorithm was used to iteratively calculate the value of the input variables by minimizing the objective function SE. For solving the optimization problem, the in-house code was used based on the MATLAB function *fminsearch*. The lower and upper bounds in the function were properly chosen to accommodate a wide range of values for each of the material properties.

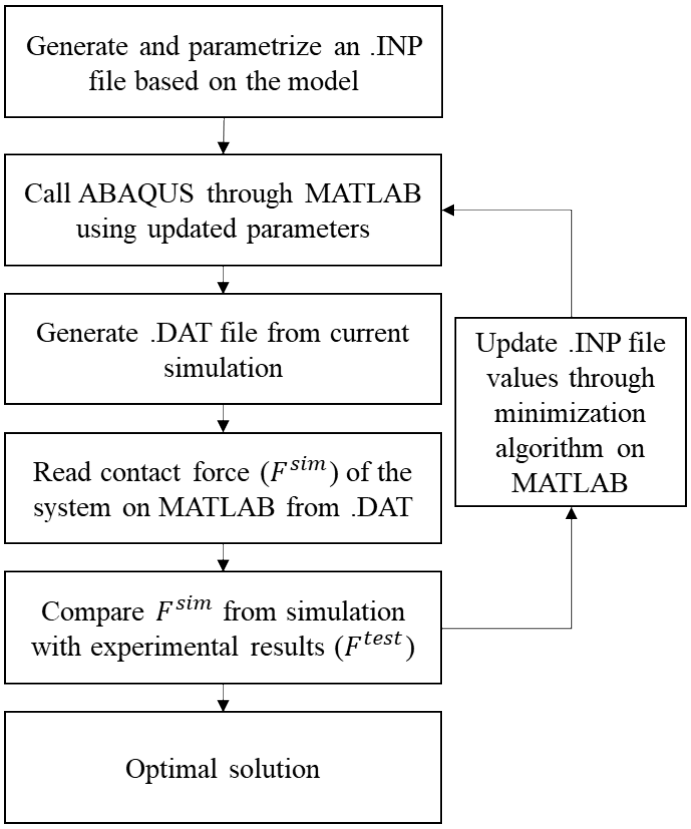

APPENDIX IV: ELASTIC MODULUS OF THE SOLID NETWORK E_S AND AGGREGATE MODULUS H_A

Once the Poisson's ratio was properly determined and set to $\nu_s = 0.17$; the elastic modulus of the solid network E_s was obtained using the fitting procedure described on Appendix III. This procedure was repeated for each of the four loading steps for every sample. Fully swollen agarose gels exhibited an elastic response with a strong correlation between stress/strain ($R^2 \approx 1$). Most studies in the literature report the aggregate modulus H_A instead of the elastic modulus of the solid network. The aggregate modulus for different agarose composition can however be obtained directly from E_s and ν_s as:

$$H_A = \frac{3(1-2\nu_s)}{2\,(1-\nu_s)} E_s \qquad 22$$

At 5% strain and before relaxation, the mean aggregate modulus values could therefore be estimated as 0.97 MPa, 1.7 MPa, and 2.43 MPa for 5%, 7.5% and 10% w/w agarose respectively. These results were in excellent agreement with the previously reported by Normand *et al.* (2000)[66]. During the compressive stage that followed stress relaxation, we further observed an increase in the aggregate modulus with respect to its initial value. In this study, H_A was observed to exponentially increase with applied deformation in the following fashion ($R^2 \approx 1$) (Figure 11):

$$H_A = a(\bar{\mu})^b + c \qquad 23$$

Values for fitting parameters were summarized in Table 3.

c_o	a	b	c
5% w/w	7.27E5	10.86	0.97
7.5% w/w	1.92E6	11.31	1.70
10% w/w	3.65E6	11.76	2.44

Table 3. Control parameters a, b, and c as a function of the agarose concentration c_o used in the samples.

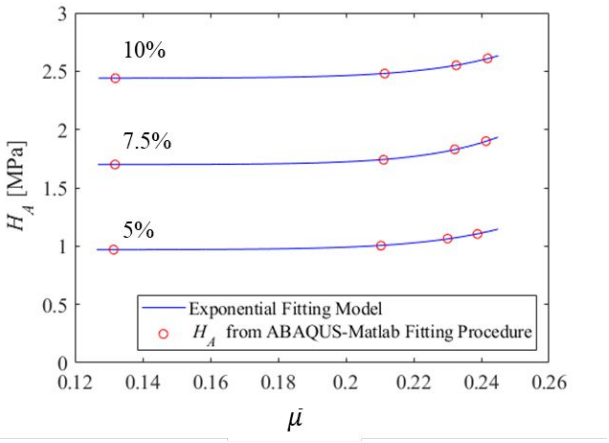

Figure 10. Evolution of the aggregate modulus H_A as a function of the second invariant of the conformation tensor $\bar{\mu}$.

The parameter c was directly related to the elastic modulus found at 5% strain (H_A^0) before the network had time to relax. This fact motivated the idea of finding the following master equation as a function of the agarose concentration c_o.

$$H_A = H_A^0\left[\frac{3}{2}10^6 c_o(\bar{\mu})^b + 1\right] \qquad 24$$

The master Equation 27 shows that agarose network becomes stiffer as the overall deformation is increased and held during large periods of time. Parameter b increases as the concentration of agarose in the samples increases. However, we found that assuming parameter b constant and equal to the average of the values shown on Table 3 ($\bar{b} = 11.3$) did not have major differences in the fitted curves shown in Figure 9.

REFERENCES

1 D. L. Kaplan, in *Biopolymers from Renewable Resources*, ed. D. L. Kaplan, Springer, Berlin, Heidelberg, 1998, pp. 1–29.
2 K. Van de Velde and P. Kiekens, *Polym. Test.*, 2002, **21**, 433–442.
3 J. Kierfeld, K. Baczynski, P. Gutjahr and R. Lipowsky, *AIP Conf. Proc.*, 2008, **1002**, 151–185.
4 T. Naghdi, H. Golmohammadi, H. Yousefi, M. Hosseinifard, U. Kostiv, D. Horák and A. Merkoçi, *ACS Appl. Mater. Interfaces*, 2020, **12**, 15538–15552.
5 M. B. Aga, A. H. Dar, G. A. Nayik, P. S. Panesar, F. Allai, S. A. Khan, R. Shams, J. F. Kennedy and A. Altaf, *Int. J. Biol. Macromol.*, 2021, **192**, 197–209.
6 J. Comaposada, B. Marcos, R. Bou and P. Gou, *Food Res. Int.*, 2018, **108**, 539–550.
7 Y. Kato, M. Iwamoto and T. Koike, *J. Cell. Physiol.*, 1987, **133**, 491–498.
8 A. L. Horwitz and A. Dorfman, *J. Cell Biol.*, 1970, **45**, 434–438.
9 J. Bnjía, M. Sittinger, P. Pitzke, E. Wilmes and C. Hammer, *ORL*, 1993, **55**, 347–351.
10 W. Megone, N. Roohpour and J. E. Gautrot, *Sci. Rep.*, 2018, **8**, 6780.
11 P. Zarrintaj, S. Manouchehri, Z. Ahmadi, M. R. Saeb, A. M. Urbanska, D. L. Kaplan and M. Mozafari, *Carbohydr. Polym.*, 2018, **187**, 66–84.
12 J. J. Roberts, A. Earnshaw, V. L. Ferguson and S. J. Bryant, *J. Biomed. Mater. Res. B Appl. Biomater.*, 2011, **99B**, 158–169.
13 L. Martikainen, K. Bertula, M. Turunen and O. Ikkala, *Macromolecules*, 2020, **53**, 9983–9992.
14 K. Bertula, L. Martikainen, P. Munne, S. Hietala, J. Klefström, O. Ikkala, and Nonappa, *ACS Macro Lett.*, 2019, **8**, 670–675.
15 O. Chaudhuri, J. Cooper-White, P. A. Janmey, D. J. Mooney and V. B. Shenoy, *Nature*, 2020, **584**, 535–546.
16 F. J. Vernerey, S. Lalitha Sridhar, A. Muralidharan and S. J. Bryant, *Chem. Rev.*, 2021, **121**, 11085–11148.
17 S. Arnott, A. Fulmer, W. E. Scott, I. C. M. Dea, R. Moorhouse and D. A. Rees, *J. Mol. Biol.*, 1974, **90**, 269–284.
18 X. Wang, R. K. June and D. M. Pierce, *J. Mech. Behav. Biomed. Mater.*, 2021, **114**, 104150.
19 A. Ed-Daoui and P. Snabre, *Rheol. Acta*, 2021, **60**, 327–351.
20 J. E. Olberding and J.-K. Francis Suh, *J. Biomech.*, 2006, **39**, 2468–2475.
21 J. E. Soussou, F. Moavenzadeh and M. H. Gradowczyk, *Trans. Soc. Rheol.*, 1970, **14**, 573–584.
22 J. Chen, D. L. Bader, D. A. Lee and M. M. Knight, in *8th International Conference on Cell & Stem Cell Engineering (ICCE)*, eds. A. El Haj and D. Bader, Springer, Berlin, Heidelberg, 2011, pp. 17–20.
23 H. M. Pauly, L. W. Place, T. L. Haut Donahue and M. J. Kipper, *Biomacromolecules*, 2017, **18**, 2220–2229.
24 D. Caccavo and G. Lamberti, *Mater. Sci. Eng. C Mater. Biol. Appl.*, 2017, **76**, 102–113.
25 D. Caccavo, S. Cascone, S. Poto, G. Lamberti and A. A. Barba, *Carbohydr. Polym.*, , DOI:10.1016/j.carbpol.2017.03.027.
26 T. Casalini, Politecnico di Milano, 2013.
27 F. J. Vernerey, R. Long and R. Brighenti, *J. Mech. Phys. Solids*, 2017, **107**, 1–20.
28 X. Wang, T. S. E. Eriksson, T. Ricken and D. M. Pierce, *J. Mech. Behav. Biomed. Mater.*, 2018, **86**, 409–422.
29 D. M. Pierce, M. J. Unterberger, W. Trobin, T. Ricken and G. A. Holzapfel, *Biomech. Model. Mechanobiol.*, 2016, **15**, 229–244.
30 Q.-M. Wang, A. C. Mohan, M. L. Oyen and X.-H. Zhao, *Acta Mech. Sin.*, 2014, **30**, 20–27.
31 Y. Hu, X. Zhao, J. J. Vlassak and Z. Suo, *Appl. Phys. Lett.*, 2010, **96**, 121904.
32 M. Galli, K. S. C. Comley, T. A. V. Shean and M. L. Oyen, *J. Mater. Res.*, 2009, **24**, 973–979.
33 D. G. T. Strange, T. L. Fletcher, K. Tonsomboon, H. Brawn, X. Zhao and M. L. Oyen, *Appl. Phys. Lett.*, 2013, **102**, 031913.
34 K. Terzaghi, *Theoretical Soil Mechanics*, John Wiley & Sons, Ltd, 1st edn., 1943.
35 O. Coussy, *Poromechanics*, John Wiley & Sons, 2004.
36 J. Bear and Y. Bachmat, in *Introduction to Modeling of Transport Phenomena in Porous Media*, Springer Netherlands, Dordrecht, 1990, pp. 43–262.
37 W. Y. Gu, H. Yao, C. Y. Huang and H. S. Cheung, *J. Biomech.*, 2003, **36**, 593–598.
38 B. Mao, A. Bentaleb, F. Louerat, T. Divoux and P. Snabre, *Food Hydrocoll.*, 2017, **64**, 59–69.
39 S. Arbabi and M. Sahimi, *Phys. Rev. B*, 1993, **47**, 695–702.
40 T. Shen, R. Long and F. Vernerey, *Comput. Mech.*, 2019, **63**, 725–745.
41 M. Watase and K. Arakawa, *Bull. Chem. Soc. Jpn.*, 1968, **41**, 1830–1834.

42 G. A. Holzapfel, *Nonlinear Solid Mechanics: A Continuum Approach for Engineering*, 2000.
43 R. Long, H. J. Qi and M. L. Dunn, *Soft Matter*, 2013, **9**, 4083–4096.
44 T. Shen, Z. Song, S. Cai and F. J. Vernerey, *Proc. Natl. Acad. Sci.*, 2021, **118**, e2105974118.
45 F. J. Vernerey, *J. Mech. Phys. Solids*, 2018, **115**, 230–247.
46 C.-Y. Hui, F. Cui, A. Zehnder and F. J. Vernerey, *Proc. R. Soc. Math. Phys. Eng. Sci.*, 2021, **477**, 20210608.
47 C. L. Lewis, K. Stewart and M. Anthamatten, *Macromolecules*, 2014, **47**, 729–740.
48 K. C. Labropoulos, S. Rangarajan, D. E. Niesz and S. C. Danforth, *J. Am. Ceram. Soc.*, 2001, **84**, 1217–1224.
49 E. H. Lee, *J. Appl. Mech.*, 1969, **36**, 1–6.
50 H. Eyring, *J. Chem. Phys.*, 1936, **4**, 283–291.
51 H. Eyring, *J. Chem. Phys.*, 1935, **3**, 107–115.
52 S. Lamont and F. J. Vernerey, *J. Appl. Mech.*, 2022, **89**, 011009.
53 T. Erdmann and U. S. Schwarz, *Phys. Rev. Lett.*, 2004, **92**, 108102.
54 U. S. Schwarz and S. A. Safran, *Rev. Mod. Phys.*, 2013, **85**, 1327–1381.
55 S. Klumpp and R. Lipowsky, *Proc. Natl. Acad. Sci.*, 2005, **102**, 17284–17289.
56 M. J. Buehler and Y. C. Yung, *Nat. Mater.*, 2009, **8**, 175–188.
57 K. Prechtel, A. R. Bausch, V. Marchi-Artzner, M. Kantlehner, H. Kessler and R. Merkel, *Phys. Rev. Lett.*, 2002, **89**, 028101.
58 M. E. Cates, *J. Phys. Chem.*, 1990, **94**, 371–375.
59 P. Thirion and J. Tassin, *J. Polym. Sci. Polym. Phys. Ed.*, 1983, **21**, 2097–2108.
60 A. Pluen, P. A. Netti, R. K. Jain and D. A. Berk, *Biophys. J.*, 1999, **77**, 542–552.
61 T. C. Laurent, *Biochim. Biophys. Acta BBA - Gen. Subj.*, 1967, **136**, 199–205.
62 E. M. Johnson, D. A. Berk, R. K. Jain and W. M. Deen, *Biophys. J.*, 1995, **68**, 1561–1568.
63 E. Fernández, D. López, C. Mijangos, M. Duskova-Smrckova, M. Ilavsky and K. Dusek, *J. Polym. Sci. Part B Polym. Phys.*, 2008, **46**, 322–328.
64 V. C. Mow, S. C. Kuei, W. M. Lai and C. G. Armstrong, *J. Biomech. Eng.*, 1980, **102**, 73–84.
65 T. Shen and F. J. Vernerey, *J. Mech. Phys. Solids*, 2020, **143**, 104028.
66 V. Normand, D. L. Lootens, E. Amici, K. P. Plucknett and P. Aymard, *Biomacromolecules*, 2000, **1**, 730–738.